

Deciphering stress perturbations throughout the 2025 M_w 7.1 Dingri, Southern Xizang Earthquake

Received: 12 June 2025

Accepted: 17 December 2025

Published online: 16 January 2026

 Check for updatesZhangfeng Ma ^{1,5}, Chenglong Li ^{2,5}, Hongyu Zeng¹, Han Chen², Mingzhe Lyu^{1,3}, Yingfeng Zhang ², Luca Dal Zilio ^{1,3}, Xinjian Shan ² & Shengji Wei⁴ 

The 2025 moment magnitude (M_w) 7.1 Dingri earthquake in Southern Xizang, China, caused severe devastation and exhibited a complex stress evolution. Its northward unilateral rupture along the twisted, west-dipping graben edge generated ~2 MPa of dynamic stress, triggering blind coseismic slip on an east-dipping fault. Coseismic stress perturbations activated over 50 previously unmapped fault segments, mostly with aseismic slip, while also inducing an early viscoelastic response in the weak middle-to-lower crustal layer below ~20 km depth. Here we explain these behaviours by deciphering the stress perturbations through earthquake cycle observations and models. A major implication is that tracking stress evolution throughout an earthquake provides critical insights into earthquake mechanics.

Earthquake rupture dynamics and their postseismic manifestations are governed by the intricate interplay between stress transfer, fault geometry and friction, as well as the rheological responses of the Earth's crust^{1–3}. While coseismic rupture represents the sudden release of accumulated elastic strain, the subsequent postseismic phase, including aftershocks, aseismic slip, and viscoelastic relaxation, provides critical insights into the mechanical behaviour of faults and the surrounding crust^{4–7}. High-resolution observations of coseismic rupture process, postseismic deformation and interseismic loading, i.e., earthquake cycle observations, are needed to resolve the stress perturbations and evolutions in and around the fault systems^{8–10}. However, three different earthquake cycle phases, including the interactions between key physical behaviours, have rarely been well-documented for fault system that hosted significant earthquakes, leaving gaps in our understanding of how these processes interconnect^{11–13}. The well-recorded 2025 M_w 7.1 Dingri earthquake, together with observations that capture critical stages of the earthquake cycle, provides a rare opportunity to investigate the complex interactions of stress perturbations during and following dynamic rupture.

The M_w 7.1 earthquake struck Dingri County, Southern Xizang, China, on January 7, 2025, causing strong ground shaking and consequent extensive infrastructure damage and 126 fatalities (https://www.chinadaily.com.cn/china/special_coverage/677cbaa1a310f1265a1d9711). The event ruptured along the Dengme Co Fault, marking the eastern boundary of the Dengme Co Graben, the southern segment of the Shenzha-Dingjie rift system¹⁴ (Fig. 1). Field investigations reported the mainshock generated fault scarps up to 3 m high and widespread en échelon tension cracks¹⁵. However, the rupture process and its interactions with its aftermath, such as aftershocks, aseismic slip, and viscoelastic relaxation remain poorly constrained.

In this work, we integrate geodetic and seismic observations to reveal that the 2025 M_w 7.1 Dingri earthquake involved a complex rupture process, widespread triggered aseismic and seismic slip, and early viscoelastic relaxation, thereby elucidating how stress transfer throughout an earthquake shapes fault behaviour. These results demonstrate that earthquake-cycle observations are essential for constraining the spatiotemporal evolution of stress and for linking rupture processes, fault interaction, and crustal rheology within a unified framework of earthquake mechanics.

¹Earth Observatory of Singapore, Nanyang Technological University, Singapore, Singapore. ²State Key Laboratory of Earthquake Dynamics and Forecasting, Institute of Geology, China Earthquake Administration, Beijing, China. ³Asian School of the Environment, Nanyang Technological University, Singapore, Singapore. ⁴Key Laboratory of Deep Petroleum Intelligent Exploration and Development, Institute of Geology and Geophysics, Chinese Academy of Sciences, Beijing, China. ⁵These authors contributed equally: Zhangfeng Ma, Chenglong Li. ✉e-mail: shjwei@gmail.com

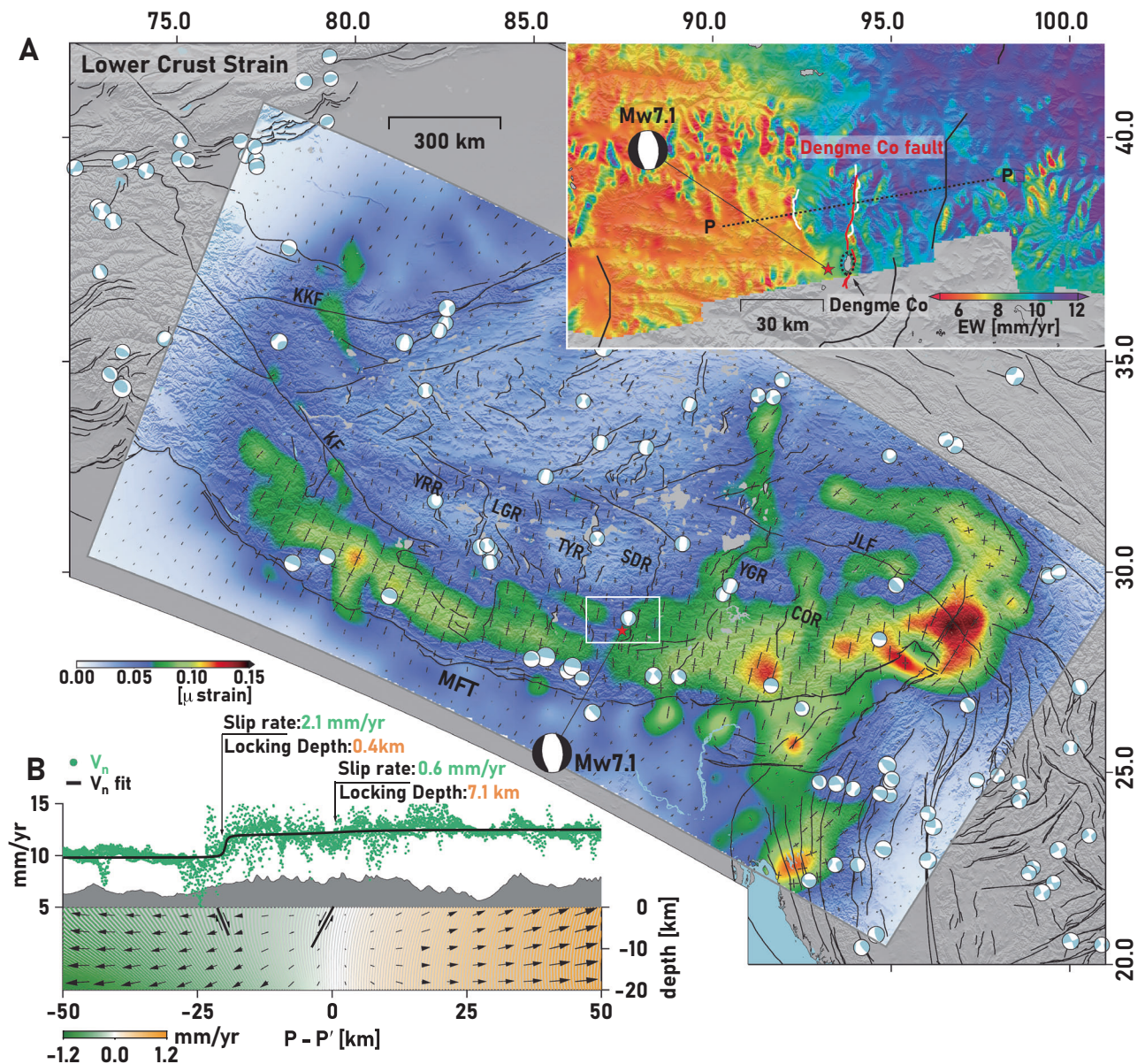


Fig. 1 | Lower crust strain rate, interseismic velocity, and locking states of two major faults. **a** Regional map showing maximum shear strain rates in the lower crust, derived from geodetic data (GNSS and InSAR), across a large region of the Tibetan Plateau. Beach balls indicate focal mechanisms of earthquakes ($M_w > 6$, 2005–2024) from the GCMT catalogue. The upper-right inset (white rectangle in **a**) zooms into the region around the M_w 7.1 Dingri earthquake and displays an east-west interseismic velocity map. The white trace in the inset represents the mapped fault trace based on co- and post-seismic deformations. The dashed black

ellipse marks Dengme Co, and the red fault trace denotes the Dengme Co Fault. YRR: Yari Rift, LGR: Lunggar Rift, TYR: Tangra-Yumco Rift, SDR: Shenzha-Dingjie Rift, YGR: Yadong-Gulu Rift, COR: Cona-Oiga Rift, MFT: Main Frontal Thrust, JLF: Jiali Fault, KKF: Karakash Fault, KF: Karakoram Fault. **b** The upper panel shows the profile of fault-normal velocity along with the corresponding velocity fit using the Okada model. The lower panel presents the forward-modelled deformation derived from the inverted lower crustal strain (from **a**).

Results

Coseismic surface deformations and interseismic loading

Interferometric SAR (InSAR) data reveal a complex coseismic deformation pattern produced by the earthquake (Fig. 2A) (**Methods**). The Line of Sight (LOS) offsets reflect a mixture of east-west and vertical motion, consistent with the normal faulting nature of the event. Sharp transitions between positive and negative displacements delineate a ~30 km long, near north-south oriented, twisted rupture trace, beginning ~15 km north of the epicentre and characterised by three eastward-protruding bends (Fig. 2A). Stronger displacements on the western side of the fault trace indicate a west-dipping fault geometry. The maximum LOS offset contrast across the fault (~2.5 m) agrees well with field measurements of 2.5–3.0 m vertical scarps¹⁴. This fault was incompletely mapped in earlier

inventories, neither by geological studies^{16,17} nor by interseismic geodetic imaging¹⁸, likely because of limited field access, subdued topography across the north-south trending valleys (Fig. 2B) and the spatial smoothing applied in previous geodetic studies^{18,19}. Although no clear surface rupture is evident near the epicentre, descending InSAR and Pixel Offset Tracking (POT) images show LOS offsets exceeding 50 cm (Supplementary Fig. S1), indicating a relatively deep, blind rupture. Similarly, at ~25 km west of the main rupture, deformation maps reveal a localised displacement pattern with peak LOS motion of ~0.6 m but no surface rupture, requiring buried slip on an east-dipping fault spatially separated from the main ruptured faults.

Interseismic loading is essential to constrain coseismic rupture behaviour and recurrence intervals. We jointly invert Global

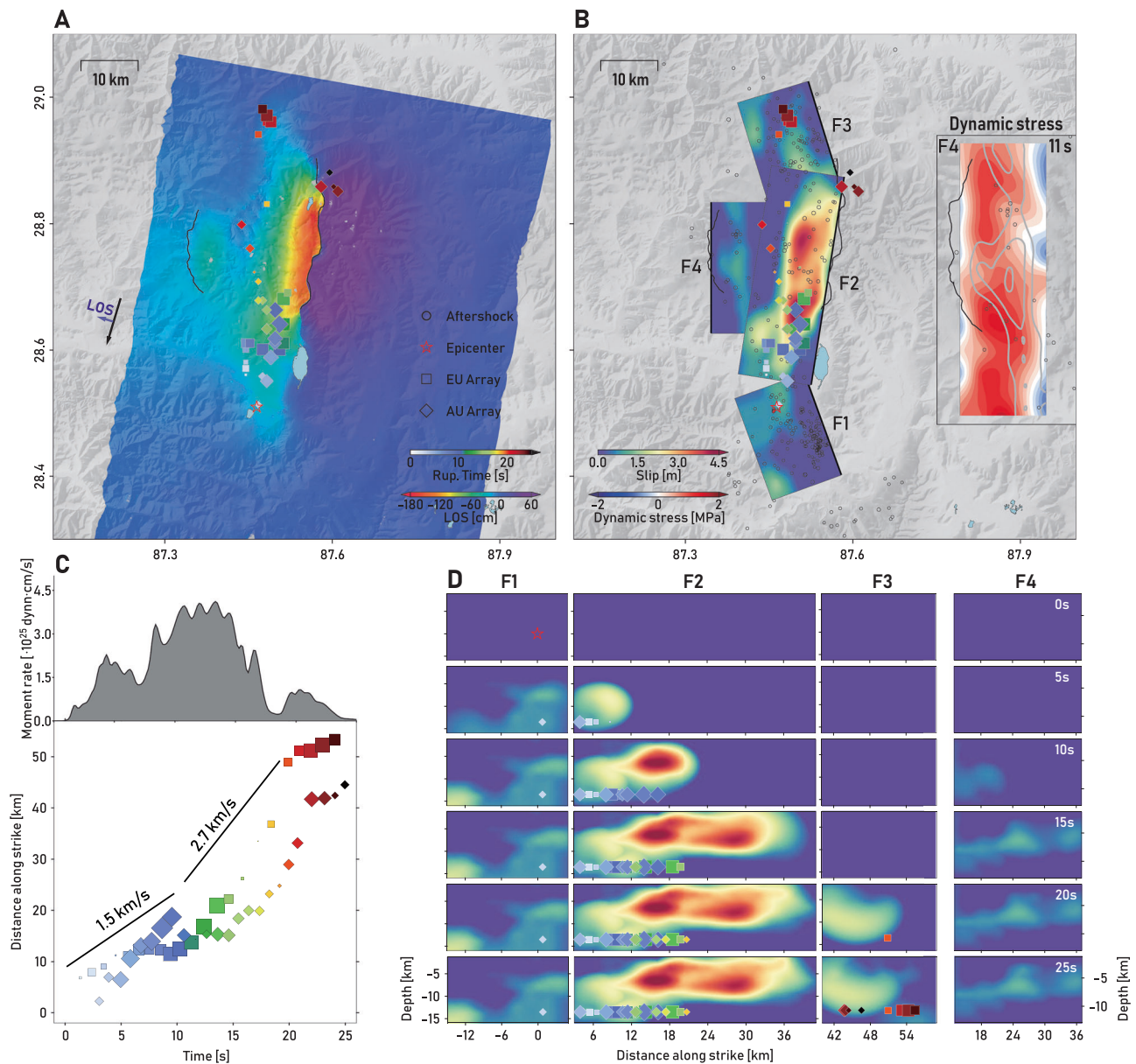


Fig. 2 | Kinematic rupture models of the M_w 7.1 Dingri earthquake and dynamic stress generated by rupture on the main fault. **a Map view of the high-frequency (HF) radiation evolution and ALOS-2 coseismic surface displacement. **b** Map view of the finite fault slip distribution, overlaid with HF radiators and relocated**

aftershocks ($M > 3$). The inset in **(b)** shows the dynamic Coulomb stress (11 s after the origin time) on F4. **c** Moment-rate function of the finite fault model and the spatiotemporal progression of HF radiation. **d** Snapshots of coseismic slip evolution and HF radiation.

Navigation Satellite System (GNSS) offsets and decadal InSAR observations (Supplementary Fig. S2–3) acquired before the Dingri earthquake to derive high-resolution 3D interseismic surface deformation rate maps for southern Xizang (Fig. 1 and Supplementary Fig. S4) (**Methods**). These maps constrain lower-crustal strain-rate models (Fig. 1A, Supplementary Fig. S5–6), which illuminate the mechanisms driving both the Dingri earthquake and the broader graben system (**Methods**). At a regional scale, east-west extensional strain in the lower crust aligns with the major grabens of southern Xizang (Fig. 1A). Locally across the Dengme Co Graben, strain distribution indicates -2.4 mm/yr of extensional deformation beneath the ruptured faults (Fig. 1B), implying a causal link between lower crustal loading/flow and the earthquake.

Independent inversions of interseismic geodetic observations across the main fault segment yield a locking depth of 7.1 ± 3.2 km and a slip rate of 0.6 ± 0.2 mm/yr (**Methods**), consistent with geological

estimates of 0.1 – 0.7 mm/yr for the Dengme Co Fault¹⁵. Assuming a -3 m coseismic slip and a fully locked fault, this corresponds to a recurrence interval of ~ 5000 years for Dingri-like events. In contrast, the western fault segment shows a locking depth of 0.4 ± 0.1 km and a slip-rate of -2.1 ± 0.2 mm/yr, indicating that shallow creep dominates the interseismic period (Fig. 1B) but the same segment also hosted deeper coseismic rupture (Fig. 2a). Such shallow creep may act as a rupture barrier, inhibiting coseismic slip from reaching the surface. A high-resolution coseismic rupture model is therefore required to clarify how interseismic loading relates to coseismic rupture and subsequent postseismic responses.

Kinematic rupture process and dynamic triggering

To resolve the spatiotemporal rupture process of the earthquake, we apply a back-projection (BP) method²⁰ to high-frequency (0.3 – 1.0 Hz) teleseismic waveforms recorded by the Australian (AU) and Eurasian

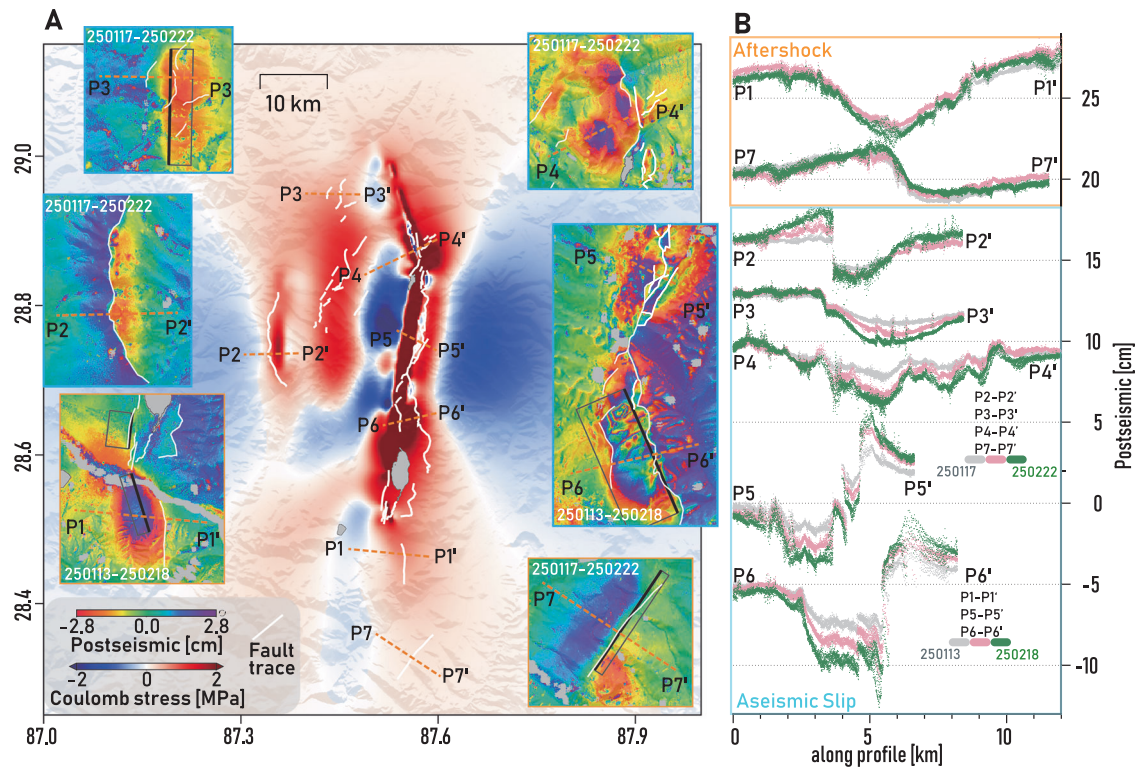


Fig. 3 | Activated potential faults after the earthquake, postseismic deformations, and static Coulomb stress. a Map view of static Coulomb stress change at 1 km depth, calculated using the finite fault model. White lines represent mapped potential fault traces. In the Coulomb stress calculation, the strike angle of all receivers is fixed at 189° , the dip angle is set to 48° , and the rake angle is -85° . The six insets in (a) show wrapped InSAR line-of-sight (LOS) data capturing postseismic deformations, along with the time pairs for the InSAR acquisitions. Our mapped

fault segment traces (white lines) and fault segments (black rectangles, with the heavier line indicating the upper bound) are used in modelling two aftershocks and three aseismic slip events. The fault planes in the inset plots correspond to our derived fault models for these aftershocks and aseismic slip events. **b** Seven profiles of postseismic deformations from (a), with aftershock-related deformations shown at the top and aseismic slip events at the bottom. The first and last dates of post-seismic SAR acquisitions are indicated in grey and green text, respectively.

(EU) arrays (Supplementary Fig. S7–8) (**Methods**). BP results reveal both the spatial distribution and temporal evolution of high-frequency radiators (Fig. 2A, C). The BP results show that rupture propagated unilaterally northward, initiating at a relatively slow speed of -1.5 km/s during the first 10 s before accelerating to -2.7 km/s and continuing for ~ 30 km. Strong high-frequency radiation in the first 10 s coincides with the region experiencing the most severe damage¹⁴. Near the northern termination of the surface rupture, a cluster of intense high-frequency radiation appears, possibly resulted from the stopping phase²¹ generated by the termination of the rupture. These BP results provide independent constraints on rupture speed, forming a critical input to the subsequent finite fault inversion.

Combining aftershock seismicity²², geodetic observations and both GCMT²³ and W-phase²⁴ moment-tensor solutions, we approximate the fault geometry with four fault segments: southern (F1), central (F2), northern (F3), and western (F4) (Fig. 2B). We jointly invert teleseismic body waves, local and regional strong motion waveforms, and down-sampled geodetic data for a finite fault model (**Methods**). Our preferred rupture model (Fig. 2) reproduces all major features in all these observations (Supplementary Fig. S9–12). The model shows that the rupture initiated on F1 at -8 km depth, with slip on F1 and the southern part of F2 concentrated between the depth of 5–10 km. This slip coincides with intense high-frequency seismic radiation (Fig. 2B), indicating the heterogeneous stress conditions at depth. The largest slip asperity occurred on the northern part of F2, with slip shallower than 7 km that reached to the surface. Despite producing the twisted surface rupture, this dominant slip patch ruptured relatively smoothly at high speed and is relatively depleted of high-frequency radiation, likely reflecting a more uniform rupture process^{25–28}.

Most of the rupture on the western fault (F4) occurred 10–15 s after the origin time, at the depths of 3–8 km (Fig. 2D). Stress transferred from the main fault rupture (F1–F3) produced dynamic Coulomb stress changes on F4 that peaked at -2 MPa also at 10–15 s (Fig. 2B and Supplementary Fig. S13), coincided with the rupture timing inferred from the finite fault model. Coseismic slip area on F4 was largely confined to the positive Coulomb stress change regime (Fig. 2B). These agreements indicate that the deeper portion of F4 was dynamically activated during the mainshock, while the shallow sections accommodated coseismic stress perturbations through postseismic afterslip (see next Section).

Widespread Triggered Aseismic and Seismic Slip

High resolution Sentinel-1 InSAR data captured postseismic deformation during the month following the mainshock (**Methods**), revealing intricate fields associated with viscoelastic relaxation, shallow aftershocks, and aseismic afterslip (Fig. 3). Viscoelastic relaxation is characterised by long-wavelength surface deformation (see next section), whereas shallow afterslip and aftershock deformations are in much shorter wavelength (Figs. 3, 4, Supplementary Fig. S14–15). The latter shallow processes can be further distinguished by their different temporal behaviours: aftershock deformation remains static in time, while aseismic slip generally continues to evolve (e.g., profiles 1,7 vs. 2–6 in Fig. 3b).

Careful inspection of the postseismic InSAR images identified two aftershocks (Supplementary Table S1) and more than 50 mostly unmapped fault segments that exhibited shallow aseismic slip (Fig. 3A, Video.S1 archived in Figshare) (**Methods**). The largest LOS displacement (~ 15 cm) occurred between January 8 and February 13, ~ 5 km

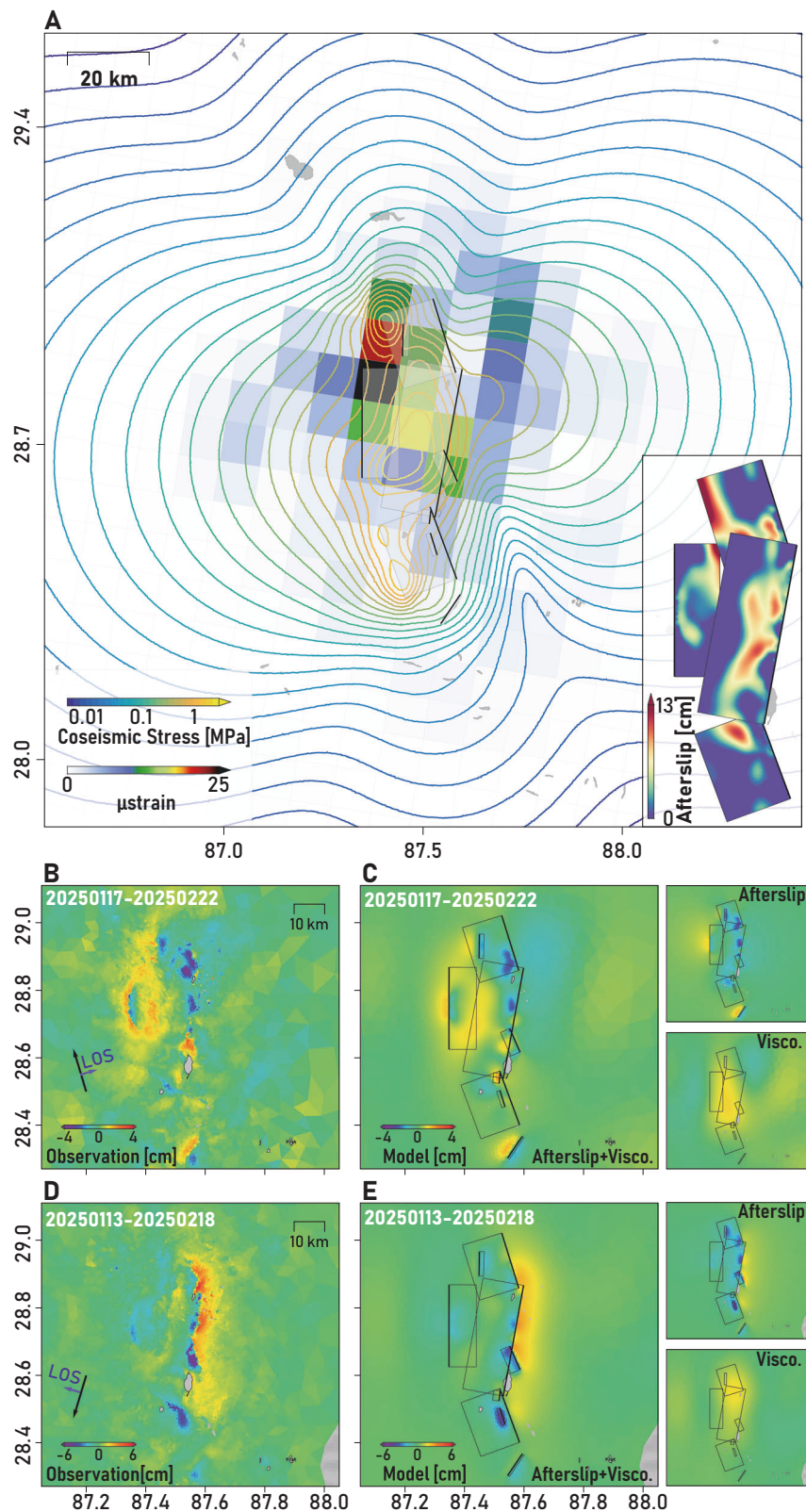


Fig. 4 | Coseismic stress change, inverted viscoelastic strain map, afterslip model, and postseismic deformation data fitting. **a** Contours represent the amplitude of coseismic stress change imposed on viscoelastic layers at depths of 20–40 km. The colour of the cuboids indicates the second invariant component of the inverted strain tensors. The map projection of fault planes used in the afterslip inversion is shown as rectangles with grey lines, with the upper bound marked by a

black line. The inset presents a map view of the afterslip model for faults F1–F4. **b–e** show ascending and descending postseismic InSAR observations and model predictions. Fault planes in **(c)** and **(e)** are displayed as rectangles, with the upper bound indicated by thick black lines. Two smaller panels next to **(c)** and **(e)** illustrate the individual contributions from afterslip and viscoelastic relaxation, respectively.

north of Dengme Co (Supplementary Fig. S14). We modelled the deformation from the two aftershocks and aseismic afterslip on three fault segments using uniform-slip Okada model (Supplementary Fig. S16–20 and Supplementary Table S1) (**Methods**). The inferred centroid depths are $\sim 2\text{--}8$ km, with slip direction showing a substantial strike-slip component, likely because the fault normal directions are misaligned with the extensional principal stress in the crust, as well as fault geometry and friction complexities inherited through geological time scale evolutions.

A striking feature of all triggered slip is their overlap with areas of large (>1 MPa) positive Coulomb stress change from the mainshock at 1 km depth (Fig. 3A). These triggered slip can be grouped into three categories, Type 1 occurred on or very close to the main ruptured faults (F2), particularly at rupture terminations and at strongly curved sections of the surface trace (the three eastward protrusions). These locations coincide with coseismic static stress perturbation exceeding 2 MPa, consistent with geometrically controlled rupture arrest and incomplete coseismic slip. Type 2 afterslip was distributed between the main fault F1-3 and F4, as well as above and south of the hypocentre. These slips occurred on pervasively distributed weak faults across the Dengme Co Graben under modest Coulomb stress changes (1–2 MPa). Such stress change is sufficient to drive both aseismic slip and seismic rupture, as suggested by the two aftershocks in Fig. 3B. Triggering of even bigger events like the Dingri mainshock maybe possible when the background stress condition is sufficient. Their frictional behaviour likely lies near the transition between velocity-strengthening and velocity-weakening regimes²⁹. Type 3 afterslip occurred on F4, representing accelerated interseismic creep at shallow depth (<3 km) under velocity-strengthening friction. At depths of 4–6 km on F4, however, seismic slip occurred due to dynamic stress perturbations, suggesting frictional properties that transition from stable to unstable. This depth-dependent change in friction is the key control on mechanical segmentation of fault slip along dip.

Time-series InSAR data reveals complex evolution of deformation from aseismic afterslip (Fig. 3B, profiles 2–6). From four post-seismic SAR image acquisitions, we derived LOS displacements for three consecutive 12-day intervals (Fig. 3B, and Supplementary Fig. S14–15). The temporal patterns differ across profiles. Along profiles 5 and 6, sharp offsets reflect substantial shallow afterslip on the main fault, whereas profiles 2–4 are dominated by long wavelength signals, primarily resulting from viscoelastic response, with smaller steps attributable to shallow creep. The superposition of viscoelastic response and afterslip produces variable differential amplitudes between time intervals. For example, along profile 4 the deformation increment during the first 12-day pair (purple vs. grey dots in Fig. 3B) exceeds that of the following pair (green vs. purple), whereas other profiles show much weaker double-difference signals. To better resolve detailed frictional properties on these faults, longer duration InSAR observations acquired in the future will make it possible. With long wavelength deformation features in the current dataset, the rheological nature of the middle-to-lower crust could be constrained.

Early viscoelastic response due to weak middle-to-lower crust

The long-wavelength uplift around the main fault zone in postseismic InSAR observations suggests a deformation process in the middle-to-lower crust, which is likely to be viscoelastic relaxation (Supplementary Fig. S14–15, and Fig. 4B, D). However, this response is entangled with shallow afterslip in the InSAR data, and distinguishing the two requires high spatiotemporal resolution postseismic observations. To separate these processes, we first inverted for afterslip using the same fault geometry as the coseismic slip model, assuming no additional deformation mechanism. This inversion achieved only 49% data–model correlation and left clear residuals around the main fault (Supplementary Fig. S21). In particular, the descending track shows

distinct long-wavelength positive residuals, suggesting a contribution from processes deeper than the seismogenic crust. Deep afterslip can be excluded as the resulted deformation polarity is opposite to this residual (Supplementary Fig. S21B3). We therefore used our finite fault model as input to test the surface displacements predicted by viscoelastic relaxation, adopting a bi-viscous Burgers rheology, while simultaneously inverting for afterslip on faults (**Methods**). The resulting model reproduces the observations well. The results suggest an optimal viscoelastic layer at depth ≥ 20 km, with a Kelvin viscosity coefficient of 5×10^{17} Pa·s (Supplementary Fig. S22), given an assumed Maxwell viscosity of 1×10^{19} Pa·s that is insensitive to the early postseismic phase.

Building on this, we implement a coupled viscoelastic and elastic inversion framework^{30,31}, using postseismic InSAR data to jointly resolve afterslip and middle-to-lower crustal strain (**Methods**). Compared with coseismic slip, the resulted afterslip is primarily concentrated in the shallower sections of the main fault, with some minor slip at depth (Fig. 4A). In contrast, viscous strain localises directly beneath the fault zone and produces long wavelength uplift in the LOS observations (Fig. 4B). The preferred model reproduces both ascending and descending observations at short and long wavelengths (Fig. 4B–E), yielding a data–model correlation of 87%, substantially higher than that from afterslip-only inversion. The lower-crustal strain distribution from this joint inversion also closely matches the forward stress field calculated from the finite fault model (Fig. 4a). Resolution tests further confirm the robustness of the inversion (Supplementary Fig. S23). Finally, trade-offs between viscoelastic relaxation and deep afterslip are ruled out, as their opposite polarity in the resulting LOS displacement.

One could argue that the observed uplift in the LOS deformation (Fig. 4B) might be resulted from poroelastic rebound in the upper crust, driven by fluid flow triggered by the mainshock^{32,33}. To test this, we calculated the volumetric stress change induced by the coseismic slip. The resulted stress field shows a clear compressional pattern within the uplifted region (Supplementary Fig. S24), corresponding to a compaction response due to coseismic slip. We then incorporated fluid diffusion and modelled three poroelastic rebound scenarios, with permeability structures extending to the depths of 5 km, 10 km, and 20 km. All scenarios predict > 3 cm of surface subsidence, opposite to the observed uplift (Supplementary Fig. S25). We therefore conclude that the poroelastic rebound alone contributed minimally to the postseismic surface deformation, and the observed long wavelength uplift is mostly from viscoelastic relaxation.

In our preferred viscoelastic model, a Kelvin viscosity of 5×10^{17} Pa·s indicates a fairly weak mid-to-lower crust beneath the Dingri earthquake. This value lies at the lower end of viscosities reported for Xizang and the adjacent regions (Supplementary Table S2). Notably, the top of this viscous layer coincides with the maximum depth of early aftershocks recorded by a local dense array (Supplementary Fig. S26). Independent seismic evidence further supports this interpretation: shear wave seismic tomography and receiver function results along east-west oriented profiles at ~ 100 km north of Dingri reveal a low-velocity zone at 20–40 km depth^{34,35} (Supplementary Fig. S27). These independent investigations all point to a weak middle-to-lower crust in the vicinity of the Dingri earthquake. Our findings are consistent with the long-standing hypothesis that the partially molten lower crust flows laterally in response to gravitational forces and crustal thickening in Southern Xizang^{36–38}. Such deep-seated flow could be responsible for driving upper crust viscous buckling and crustal extension in Southern Xizang^{39–41}.

Methods

Coseismic displacement map processing

We used CtSent software to process Sentinel-1 InSAR interferograms (see Supplementary Table S3). We first completed the geometrical

coregistration⁴² and then corrected the azimuth misregistration⁴³ of all images. We simulated the flattened earth and topographic phase and removed from all interferograms. We performed multi-looking operation on all interferograms using a window size of 5×2 (range-by-azimuth). Then an adaptive spectral filter was applied⁴⁴. We masked pixels with coherence < 0.75 and built an All-Pair-Shortest-Path (APSP) network⁴⁵ using phase gradients to unwrap single-interferogram phases while excluding edges with large gradients (e.g., across faults). All unwrapped interferograms were geocoded at $-25 \text{ m} \times 25 \text{ m}$ (Supplementary Fig. S1).

We processed ALOS-2 Stripmap data using ISCE software. A 1×2 multilook (range-by-azimuth) preserved resolution for phase unwrapping, and the same adaptive spectral filtering was applied. We applied ionospheric correction to ALOS-2 data using a 32×64 multilook to enhance signal-to-noise-ratio (SNR) and prevent unwrapping-induced artifacts from the split-spectrum method⁴⁶. All interferograms were then geocoded (Supplementary Fig. S1).

We performed Pixel Offset Tracking (POT) on Sentinel-1 and ALOS-2 images using ISCE's `ampcor.py`, with 128-pixel windows and a 4-pixel step. Results were Gaussian-filtered (5×5) and masked for correlations < 0.6 . All POT results are shown in Supplementary Fig. S1.

Time series InSAR data processing

We obtained filtered interferograms from the COMET LiCSAR platform⁴⁷ (Supplementary Table S4), already corrected for topography and flat-earth effects. After applying GACOS atmospheric corrections⁴⁸, we removed interferograms with mean coherence < 0.75 and retained pixels with average coherence > 0.75 . We computed temporal coherence and masked pixels below 0.75 before APSP-based phase unwrapping refined by coherence quality. Interferograms were referenced to the first acquisition, and velocities were estimated via iterative reweighted least squares, incorporating a Heaviside jump for $Mw > 5$ events to minimise the coseismic effects.

After velocity estimation, we corrected for rigid plate motion by removing rotation rate of the Eurasian plate from the velocity fields. We further aligned InSAR velocities to a Eurasia-fixed GNSS frame by fitting a second-degree polynomial to remove orbital ramps and constant offsets. This deramping effectively mitigates residual orbital ramps and offsets but also removes the long-wavelength vertical component. Consequently, in the plastic strain and fault locking analyses, we used levelling data as vertical constraints instead of InSAR-derived vertical velocities (see next sections). The ascending and descending track velocity maps are shown in Supplementary Fig. S2. A comparison between the final InSAR velocity maps and GNSS velocities is presented in Supplementary Fig. S3.

3D interseismic velocity map, slip rate and locking depth

Decomposing 3D velocities from ascending and descending InSAR data requires additional constraints, as polar-orbiting satellites poorly resolve North–South motion. Interpolating the N–S velocity helps reduce degrees of freedom but may oversmooth fault-related deformation, biasing 3D estimates. To address this, we used the interpolated velocity azimuth angle (Supplementary Fig. S28), referenced to a Eurasia-fixed frame, as an additional constraint instead of directly interpolating the North–South velocity^{49,50}. Supplementary Fig. S4 shows the 3D interseismic velocity fields, with GNSS comparison in Supplementary Fig. S29. High correlations (0.96 E–W, 0.88 N–S) confirm its robustness, and uncertainties of all components were also estimated. These uncertainties are derived from the diagonal elements of the inverse of the normal matrix, i.e., from the linear inversion of $BX = L$, where B is the design matrix and L the combined ascending and descending LOS observations. The uncertainties correspond to the square roots of the diagonal elements of $inv(B^T B)$. Our results in Supplementary Fig. S30A–C show: the East–West direction has the lowest uncertainty; the Up–Down follows; the North–South direction

has the highest uncertainty. Regions with overlapping swaths exhibit the lowest uncertainties due to better geometric constraints provided by multiple viewing angles. This directional variation in uncertainty may help explain the relatively lower InSAR–GNSS correlation in the North–South component.

We also computed the residual misfit of the inversion using $V = BX - L$. The root mean square (RMS) misfit is calculated as $\sqrt{\frac{V^T V}{n-1}}$, where n is the number of observations. This metric quantifies the disagreement between overlapping InSAR tracks. Our results (Supplementary Fig. S30d) show that the RMS misfit is generally less than 3 mm/yr, indicating good consistency among different track combinations.

To estimate the slip rate and locking state of the main fault and F4 segment, we extracted the horizontal velocity along the profile in Fig. 1 and converted them into the fault-normal direction. Due to the potential glacier motion and landslides related deformation in our horizontal velocity map (Fig. 1 and Supplementary Fig. S4), we adopted a simplified Okada model⁵¹ to represent the interseismic velocity along the two faults. Each fault is modelled as a dipping segment characterised by its fixed surface trace, locking depth (starting point depth), down-dip width, and slip rate. We set a large down-dip width of 150 km to approximate a deep creeping extension, about three times half of the profile extent. We used a Markov Chain Monte Carlo (MCMC) process to search the final four parameters and a constant offset. The final fit results are presented as Fig. 1B.

Interseismic lower crust strain (Plastic Strain) inversion

We inherited the same framework as introduced in Wang and Barbot⁵² to invert the lower crust strain. We first collected 4458 GNSS horizontal velocity vectors and 532 levelling measurements from multiple studies^{53–55}, and masked out all observations out of cuboid region. The finally involved 617 GNSS horizontal velocity vectors are relative to the fixed Eurasia plate. All levelling data are relative to the stable sites northeast of the Tibet Plateau. To better approximate the movement of the Tibet Plateau, we first removed the net rotation in GNSS vectors⁵².

Through least square fitting, we estimated the Euler pole and angular velocity and removed the forwarded net rotation from the GNSS horizontal velocity vectors (Supplementary Fig. S31A). We also calculated the rotation content and removed them from InSAR horizontal velocity maps (Supplementary Fig. S31B–C). We inherited the assumption that these deformations free of net rotations are caused by stratified lithosphere beneath the Tibet Plateau⁵². The accumulated slip of faults, strain in the lower crust and upper mantle can contribute to the observed surface deformation^{31,56}. Following Wang and Barbot⁵², we discretize all faults in triangle dislocations⁵⁷ and their bottom reach the brittle-ductile transition provided by CRUST1.0⁵⁸. We approximated the ductile layers with a size of 2500 km width by 1250 km length along the strike angle of 28 degrees, which is same as the convergence direction of the Indian Plate and Eurasia Plate, using discretized cuboids with 50 km length. There are 1250 cuboids, with $1250 \times 6 = 7800$ strain elements to be solved. The bottom depth of all cuboids is set to the Moho⁵⁸, with a uniform thickness of 20 km. In the simultaneous inversion of fault slip and cuboid strain elements, we performed Laplacian smoothing on their respective layers. To enforce the deviatoric strain to be constant in the lithosphere, we set an additional constraint to the trace of strain tensor to be zero.

Dense InSAR velocity maps were incorporated as additional constraints beyond Wang and Barbot⁵². The green functions including the brittle and ductile ones are in the larger scale. To invert this large-scale geodetic problem, we convert the objective function from least squares to quadratic programming⁵⁹. The mathematical formulation of

this geodetic inversion $V = GX$ is given by

$$\begin{bmatrix} V_{ew} \\ V_{ns} \\ V_{level} \\ V_{InSAR_{ew}} \\ V_{InSAR_{ns}} \end{bmatrix} = \frac{\begin{bmatrix} G_f & G_s & G_l \end{bmatrix}}{G} \begin{bmatrix} f \\ S \\ \Delta_{level} \end{bmatrix} \quad (1)$$

where V_{level} is the levelling data, $V_{InSAR_{ew}}$ and $V_{InSAR_{ns}}$ correspond to downsampled intersismic horizontal velocity map in 500 m resolution, G_f is the green function for fault slips f , G_s is the green function for strain tensors G_s , and G_l is to accommodate the regional uplift or subsidence Δ_{level} in levelling data.

In previous studies, the inversion is completed by a regularised least-squares through solving $\begin{bmatrix} V \\ 0 \end{bmatrix} = \begin{bmatrix} G \\ \gamma^*L \end{bmatrix} X$, where γ is the regularisation factor and L is the Laplacian matrix. We converted this question into a quadratic programming problem through searching the optimal solution of

$$\begin{aligned} & \min \frac{1}{X} \left(\frac{1}{2} X^T H X + c^T X \right) \\ & \text{subject to} \\ & H = G^T G + L^T L \\ & c = -G^T V \\ & A X = 0 \\ & l o \leq X \leq u p \end{aligned} \quad (2)$$

where H is the quadratic objective matrix, c is the linear objective vector, A is the constraint matrix to set the trace of strain tensors to be zero, $l o$ is the lower boundary of X and $u p$ is their upper boundary. Supplementary Fig. S5–S6 present the model fits and residuals. Figure 1A shows the estimated maximum shear strain and horizontal orientations. Supplementary Fig. S32 shows the comparison between the lower crust strain presented in the previous study⁵². Resolution test of our lower crust strain model in the following section can illustrate our model constrained from more dense observations has good resolution.

Tele-seismic back-projection

We resolved the evolution of high-frequency (HF, 0.3–1.0 Hz) radiation of the Dingri Mw 7.1 mainshock using back-projection (BP) technique⁶⁰. BP takes advantage of source-receiver reciprocity and back-propagates the array HF waveform data to the source region, tracing the location and time of sources by either maximising the stacking power in time domain⁶¹ the coherence in frequency domain⁶². The waveform data (Supplementary Fig. S8) used for BP analysis are downloaded from two large-aperture teleseismic arrays, the Australian and Eurasian arrays (Supplementary Fig. S7) onto the mainshock source region to image the source process of the mainshock. We then adopt the MULTIPLE SIGNAL CLASSIFICATION (MUSIC)^{20,62} method to conduct BP.

Finite fault inversion of kinematic rupture model

We derived the finite fault model of the kinematic rupture process using a non-linear joint inversion of seismic waveforms and static deformation data⁶³. The seismic datasets include teleseismic P (45 stations) and SH (27 stations) waves, as well as regional strong motion (7 stations) records. Teleseismic waveform data were obtained from IRIS and recorded by the Global Seismological Network (GSN). Instrument responses were removed, and the data were converted to displacement after applying a 1.0 Hz low-pass filter. Three-component

waveform records from 7 regional strong motion stations were also incorporated (Supplementary Fig. S9).

For the static constraints, we used the ALOS-2 descending interferogram (acquired 2025-01-07), which captures the coseismic deformation with minimal postseismic contribution and full spatial coverage. One Sentinel-1 ascending interferogram was also included. Other geodetic datasets were excluded due to redundancy or significant postseismic contamination. Both ascending and descending datasets were downsampled to ~3000 points. Strong-motion and static Green's functions were computed using a 1-D velocity model⁶⁴ and a wavenumber-frequency integration method⁶⁵.

The kinematic rupture model was parameterised with four segments, defined by surface rupture traces, geodetic observation, and aftershock seismicity. Segment strikes follow the main surface rupture (F2), hinge-line (F1, F3) and postseismic creep (F4). All segments were assigned a dip of 48 degrees (including F4), consistent with both GCMT and W-phase solutions. Each fault segment was subdivided into 2 km × 2 km subfaults, with slip amplitude, rake, risetime and rupture velocity solved for on each patch. Rake was constrained between -45° and -135° . Risetime was modelled as a cosine arc, ranging from 0.75 to 7.5 s in 0.75 s steps. Slip amplitude was bounded between 0 to 6 m and the rupture velocity between 1.5 km/s to 3.0 km/s. During inversion, we set the empirical weight for the geodetic misfits to be double of that of the waveform misfits, following the previous studies⁶⁶. The preferred finite fault model is shown in Fig. 2. Fits to strong-motion and teleseismic data are presented in Supplementary Fig. S10–S11, while static deformation fits are provided in Supplementary Fig. S12.

Dynamic stress calculation and triggering potential analysis

To assess the dynamic stress on segment F4, we used the finite fault model of segments F1–F3 as sources to simulate waveforms and resulting stresses on F4. Following Haskell's (1964) double-couple radiation pattern theory⁶⁷, we computed radiation coefficients using each segment's strike, dip, rake, and relative azimuth, and scaled them by seismic moment to obtain source amplitudes. The same 1D velocity model and Green's functions as in the finite fault inversion were applied, and the source amplitudes were convolved with a cosine time function to generate synthetic displacement waveforms⁶⁵.

We performed spatial differentiation of the displacement waveforms and calculated the stress tensors. We projected those stress tensors to the traction on the receiver fault to calculate the normal and shear change (Supplementary Fig. S13A–B). The shear modulus was set to 30 GPa, and the friction coefficient was assigned a value of 0.4. We defined negative normal stress as indicative of tension. The rake angle was fixed at -85° , the averaged rake angle of the F4 finite fault slip model, with positive shear stress signifying promotion of slip in that direction. Finally, we computed the dynamic Coulomb stress change induced by the source fault on the receiver fault (Supplementary Fig. S13C).

Postseismic InSAR deformation processing and potential fault segment mapping

We produced all Sentinel-1 postseismic interferograms using CtSent software. We applied all images (Supplementary Table S5) with the same data processing steps as coseismic interferogram processing. After all data processing steps, we applied an additional atmospheric noise correction method to all postseismic interferograms, due to the contamination of heavy atmospheric noise.

In the atmospheric noise estimation process of each interferogram, we used a sliding window of the wavelength of 100 km to fit the 1D correlation between InSAR phase and elevation⁶⁸. Note that the 100 km wavelength we used is to reserve the potential long wavelength deformation in interferograms.

We modelled the InSAR phase–elevation correlation as $y = a * x + b$, where y is phase and x is elevation, estimating spatial distributions of

slope a and intercept b through sliding-window fitting. The fitted atmospheric phase \hat{y} was removed from all interferograms. As shown in Supplementary Fig. S14, the postseismic deformation snapshots reveal progressive afterslip and possible viscoelastic relaxation, distinguishing temporally evolving aseismic slip from static seismic offsets. Fig. S15 further shows overlapping short- and long-wavelength deformation patterns.

By tracking postseismic deformation through time, we identified fault segment extensions from zones of strong deformation gradients visible in at least one InSAR track. These gradients mark active faulting near the surface and were integrated with fault traces from Bayesian slip inversion (Supplementary Video S1).

Bayesian slip inversion of aftershocks and aseismic fault slip

The postseismic InSAR deformation field includes contributions from two moderate aftershock and three visually identifiable aseismic fault slip events that occurred off the main fault. We employ a Bayesian inversion approach using Geodetic Bayesian Inversion Software (GBIS)⁶⁹ to simulate these deformations. The mean deformation field from three postseismic deformation maps was inverted after semi-variogram noise estimation and quadtree subsampling. In Supplementary Fig. S16–S20 we show the posterior PDFs for the nine fault source parameters obtained after 1×10^6 iterations (burn-in calculations of the first 2×10^4 iterations are removed) and data fits and their derived optimal fault plane. The maximum a posteriori probability solution and the 95% confidence intervals are reported as Supplementary Table S1.

Geodetic afterslip and viscoelastic strain inversion

We modelled surface deformation using elastic dislocation theory in a homogeneous half-space (rigidity = 30 GPa, Poisson's ratio = 0.25), adopting the finite-fault geometry with depth extension and patch sizes increasing from -500 m near the surface by a factor of 1.1 with depth. Before inversion, we forwarded and removed the contribution from two possible aftershocks. We selected postseismic deformation data exclusively from Sentinel-1 ascending track (2025-01-17 to 2025-02-22) and Sentinel-1 descending track (2025-01-13 to 2025-02-18), assuming that the four-day observation difference between these datasets was negligible.

We inverted InSAR-derived postseismic deformation for fault afterslip using quadratic programming, constraining dip-slip to keep the rake between -135° and -45° , and applying Laplacian smoothing within and between the three fault segments (F1–F3). We set the smoothing factor to 0.045, inherited from Ma et al.²⁸. The corresponding postseismic deformation fits are presented in Supplementary Fig. S21. The data-model correlation only reaches 49%. The residuals shown in Supplementary Fig. S21a3, b3 for the ascending and descending track data all show clear residuals around the fault planes. For the descending track, clear positive residuals can be seen, indicating possible another mechanism.

We also conducted an inversion of InSAR-derived postseismic deformation to estimate both fault afterslip and lower crustal strain. In this inversion, we set the cuboid size to 10 km, given that the postseismic deformation was adaptively downsampled to samples with the highest sampling resolution of 100 m. The top depth of the lower crust was fixed at 20 km based on tests from viscoelastic relaxation forward modelling, while the bottom depth was set to 69 km, following the crustal thickness defined in the CRUST1.0 model.

We applied the same quadratic programming approach to estimate both fault afterslip and strain tensors. Incorporating lower-crustal strain significantly improves the fit, yielding a data-model correlation of 87% (65% from afterslip and 22% from lower-crustal strain) for the postseismic deformation (Fig. 4C, E), compared to the case with afterslip alone. The deformation (Fig. 4C, E) predicted from lower-crustal strain (Supplementary Fig. S33) reproduces the residual

patterns left by the afterslip-only model (Supplementary Fig. S34), providing clear evidence for a lower-crustal contribution. Moreover, the associated surface deformation (Fig. 4C, E) exhibits a much longer wavelength than that from afterslip, consistent with a plausible contribution from an early viscoelastic response.

To validate this interpretation, we compared the inferred strain amplitudes with forward-modelled viscoelastic relaxation results, which provide an independent estimate based solely on forward simulations of the response to static coseismic stress changes. The inverted and the simulated surface deformations exhibited a similar distribution, particularly in the uplift pattern directly beneath the main fault zone (Supplementary Fig. S35).

Viscoelastic relaxation forward simulation

In viscoelastic relaxation forward simulation, the coseismic slip model from the finite fault inversion is utilised as an input to compute the associated stress field. We adopted a Burgers body (Kelvin + Maxwell elements) with a fixed Maxwell viscosity of 10^{19} Pa·s, given limited postseismic constraints. Using a simplified rheological structure for Dingri, we tested varying elastic-layer depths and Kelvin viscosities by simulating and removing viscoelastic deformation before afterslip inversion and evaluating the residuals (Supplementary Fig. S22).

Our preferred model includes a 20 km elastic upper crust over a 49 km viscoelastic layer (from CRUST1.0), consistent with the aftershock depth cutoff indicating the brittle–ductile transition. The model spans 250×250 km, and minimising residual misfit yields a Kelvin viscosity of 5×10^{17} Pa·s, lower than values from previous Tibetan studies on different earthquakes and lake loading in the Tibet Plateau (Supplementary Table S2), suggesting a weak lower crust and a proxy of the lower crust channel flow^{36,40,41}. The supportive evidence can be found from the seismic tomograph results^{34,35}. There is a low velocity zone beneath the Dingri county (Supplementary Fig. S27). Its top depth is approximately 20 km, and its thickness is around 20 km, well consistent with our preferred middle-to-lower crust model. The corresponding model-predicted surface displacements are presented in Supplementary Fig. S35. Overall, the model predictions exhibit a reasonable agreement with the InSAR observations. The most prominent feature is the localised uplift around the main fault zone.

Resolution test on the geodetic inversion

We first performed checkerboard tests to evaluate the resolution of our lower crustal strain model (Supplementary Fig. S23, S36). The results indicate that, regardless of whether we inverted fine or coarse strain distributions, regions constrained by the combined InSAR, GNSS and levelling data are well resolved. In contrast, using only GNSS data as constraints leads to a reduction in the strain model's resolution. This indicates that the additional constraints from levelling and InSAR data significantly enhance the resolution of the lower crustal strain model, making it more reliable and robust compared to models with fewer constraints. Next, we conducted checkerboard tests for the afterslip inversion, inputting strain models and afterslip distributions with varying resolutions. Our model effectively resolves these inputs in the regions with dense InSAR measurements, indicating that the observed afterslip and postseismic can be untangled and the derived lower crustal strain are reliable.

Data availability

All Sentinel-1 SAR images are provided by the European Space Agency and can be obtained from (<https://search.asf.alaska.edu/#/search>). The teleseismic data are freely provided by (<https://ds.iris.edu/ds/nodes/dmc/data/>). Our InSAR inter-, co- and post-seismic deformation maps, BP results, lower crust strain maps, mapped fault trace, kinematic coseismic slip, afterslip models, and the animation for mapped fault segments and postseismic deformations (Video. S1) are available at (<https://doi.org/10.6084/m9.figshare.30472607.v2>).

Code availability

CtSent software can be downloaded from (<https://zenodo.org/records/10776079>). ISCE software is freely accessed from (<https://github.com/isce-framework/isce2>).

References

- Wesnousky, S. G. Predicting the endpoints of earthquake ruptures. *Nature* **444**, 358–360 (2006).
- Wang, K., Hu, Y. & He, J. Deformation cycles of subduction earthquakes in a viscoelastic Earth. *Nature* **484**, 327–332 (2012).
- Taufiqurrahman, T. et al. Dynamics, interactions and delays of the 2019 Ridgecrest rupture sequence. *Nature* **618**, 308–315 (2023).
- Avouac, J.-P. From geodetic imaging of seismic and aseismic fault slip to dynamic modeling of the seismic cycle. *Annu. Rev. Earth Planet. Sci.* **43**, 233–271 (2015).
- Sun, T. et al. Prevalence of viscoelastic relaxation after the 2011 Tohoku-oki earthquake. *Nature* **514**, 84–87 (2014).
- Meng, L. et al. Earthquake in a Maze: compressional rupture branching during the 2012 Mw 8.6 Sumatra Earthquake. *Science* **337**, 724–726 (2012).
- Xu, X. et al. Surface deformation associated with fractures near the 2019 Ridgecrest earthquake sequence. *Science* **370**, 605–608 (2020).
- Harris, R. A., Simpson, R. W. & Reasenber, P. A. Influence of static stress changes on earthquake locations in southern California. *Nature* **375**, 221–224 (1995).
- Freed, A. M. Earthquake triggering by static, dynamic and post-seismic stress transfer. *Annu. Rev. Earth Planet. Sci.* **33**, 335–367 (2005).
- Wallace, L. M., Fagereng, Å & Ellis, S. Upper plate tectonic stress state may influence interseismic coupling on subduction megathrusts. *Geology* **40**, 895–898 (2012).
- Kaneko, Y., Avouac, J.-P. & Lapusta, N. Towards inferring earthquake patterns from geodetic observations of interseismic coupling. *Nat. Geosci.* **3**, 363–369 (2010).
- Bürgmann, R. The geophysics, geology and mechanics of slow fault slip. *Earth Planet. Sci. Lett.* **495**, 112–134 (2018).
- Dal Zilio, L., Hetényi, G., Hubbard, J. & Bollinger, L. Building the Himalaya from tectonic to earthquake scales. *Nat. Rev. Earth Environ.* **2**, 251–268 (2021).
- Xu, X., Wang, S., Cheng, J. & Wu, X. Shaking the Tibetan Plateau: Insights from the Mw 7.1 Dingri earthquake and its implications for active fault mapping and disaster mitigation. *npj Nat. Hazards* **2**, 16 (2025).
- Shi, F. et al. Seismogenic fault and coseismic surface deformation of the Dingri Ms 6.8 earthquake in Xizang, China. *Seismol. Geol.* **47**, 1–15 (2025).
- Wu, X. et al. The China Active Faults Database (CAFD) and its web system. *Earth Syst. Sci. Data* **16**, 3391–3417 (2024).
- Tapponnier, P. & Molnar, P. Active faulting and tectonics in China. *J. Geophys. Res.* (1896-1977) **82**, 2905–2930 (1977).
- Chen, H. et al. Large-scale extensional strain in Southern Tibet from sentinel-1 InSAR and GNSS Data. *Geophys. Res. Lett.* **51**, e2024GL110512 (2024).
- Wang, H., Wright, T. J., Liu-Zeng, J. & Peng, L. Strain rate distribution in south-central Tibet from two decades of InSAR and GPS. *Geophys. Res. Lett.* **46**, 5170–5179 (2019).
- Zeng, H., Wei, S. & Rosakis, A. A travel-time path calibration strategy for back-projection of large earthquakes and its application and validation through the segmented super-shear rupture imaging of the 2002 Mw 7.9 Denali Earthquake. *J. Geophys. Res.: Solid Earth* **127**, e2022JB024359 (2022).
- Wei, S. et al. Simultaneous rupture propagation through fault bifurcation of the 2021 Mw7.4 maduo earthquake. *Geophys. Res. Lett.* **49**, e2022GL100283 (2022).
- Yao J. et al. A Preliminary catalog of early aftershocks following the 7 January 2025 MS6.8 Dingri, Xizang Earthquake. *J. Earth Sci.* **36**, 856–860 (2025).
- Ekström, G., Nettles, M. & Dziewoński, A. M. The global CMT project 2004–2010: Centroid-moment tensors for 13,017 earthquakes. *Phys. Earth Planet. Inter.* **200-201**, 1–9 (2012).
- Hayes, G. P., Rivera, L. & Kanamori, H. Source inversion of the w-phase: real-time implementation and extension to low magnitudes. *Seismol. Res. Lett.* **80**, 817–822 (2009).
- Simons, M. et al. The 2011 Magnitude 9.0 Tohoku-Oki earthquake: mosaicking the megathrust from seconds to centuries. *Science* **332**, 1421–1425 (2011).
- Lay T. et al. Depth-varying rupture properties of subduction zone megathrust faults. *J. Geophys. Res.: Solid Earth* **117**, (2012).
- Avouac, J.-P., Meng, L., Wei, S., Wang, T. & Ampuero, J.-P. Lower edge of locked Main Himalayan Thrust unzipped by the 2015 Gorkha earthquake. *Nat. Geosci.* **8**, 708–711 (2015).
- Ma, Z. et al. Slow rupture in a fluid-rich fault zone initiated the 2024 Mw 7.5 Noto earthquake. *Science* **385**, 866–871 (2024).
- Wei, M., Kaneko, Y., Liu, Y. & McGuire, J. J. Episodic fault creep events in California controlled by shallow frictional heterogeneity. *Nat. Geosci.* **6**, 566–570 (2013).
- Moore, J. D. P. et al. Imaging the distribution of transient viscosity after the 2016 Mw 7.1 Kumamoto earthquake. *Science* **356**, 163–167 (2017).
- Barbot, S. Mantle flow distribution beneath the California margin. *Nat. Commun.* **11**, 4456 (2020).
- Hu, Y., Bürgmann, R., Freymueller, J. T., Banerjee, P. & Wang, K. Contributions of poroelastic rebound and a weak volcanic arc to the postseismic deformation of the 2011 Tohoku earthquake. *Earth, Planets Space* **66**, 106 (2014).
- Fialko Y. et al. Evidence of fluid-filled upper crust from observations of postseismic deformation due to the 1992 M7.3 Landers earthquake. *J. Geophys. Res.: Solid Earth* **109**, (2004).
- Shi, D., Klemperer, S. L., Shi, J., Wu, Z. & Zhao, W. Localized foundering of Indian lower crust in the India–Tibet collision zone. *Proc. Natl. Acad. Sci.* **117**, 24742–24747 (2020).
- Li, D., Tian, X., Liang, X. & Nie, S. Different formation modes of the north–south-trending rifts in southern Tibet: implications from ambient noise tomography. *Geophys. Res. Lett.* **51**, e2024GL108254 (2024).
- Clark, M. K. & Royden, L. H. Topographic ooze: Building the eastern margin of Tibet by lower crustal flow. *Geology* **28**, 703–706 (2000).
- Beaumont C., Jamieson R. A., Nguyen M. H. & Medvedev S. Crustal channel flows: 1. Numerical models with applications to the tectonics of the Himalayan-Tibetan orogen. *J. Geophys. Res.: Solid Earth* **109**, (2004).
- Li, S. et al. Partial melt or aqueous fluid in the mid-crust of Southern Tibet? Constraints from INDEPTH magnetotelluric data. *Geophys. J. Int.* **153**, 289–304 (2003).
- Bischoff, S. H. & Flesch, L. M. Normal faulting and viscous buckling in the Tibetan Plateau induced by a weak lower crust. *Nat. Commun.* **9**, 4952 (2018).
- McKenzie, D., Nimmo, F., Jackson, J. A., Gans, P. B. & Miller, E. L. Characteristics and consequences of flow in the lower crust. *J. Geophys. Res.: Solid Earth* **105**, 11029–11046 (2000).
- Hopper, J. R. & Buck, W. R. The effect of lower crustal flow on continental extension and passive margin formation. *J. Geophys. Res.: Solid Earth* **101**, 20175–20194 (1996).
- Sansosti, E., Berardino, P., Manunta, M., Serafino, F. & Fornaro, G. Geometrical SAR image registration. *IEEE Trans. Geosci. Remote Sens.* **44**, 2861–2870 (2006).
- Ma, Z., Jiang, M., Zhao, Y., Malhotra, R. & Yong, B. Minimum spanning tree co-registration approach for time-series sentinel-1 TOPS

- data. *IEEE J. Sel. Top. Appl. Earth Observations Remote Sens.* **12**, 3004–3013 (2019).
44. Goldstein, R. M. & Werner, C. L. Radar interferogram filtering for geophysical applications. *Geophys. Res. Lett.* **25**, 4035–4038 (1998).
 45. Ma Z. F., Jiang M., Khoshmanesh M. & Cheng X. Time series phase unwrapping based on graph theory and compressed sensing. *IEEE Trans. Geosci. Remote Sens.* **60**, 1–12 (2021).
 46. Liang, C. & Fielding, E. J. Interferometry with ALOS-2 full-aperture ScanSAR data. *IEEE Trans. Geosci. Remote Sens.* **55**, 2739–2750 (2017).
 47. Lazecký M. et al. LiCSAR: An Automatic InSAR Tool for measuring and monitoring tectonic and volcanic activity. *Remote Sensing* **12**, 2430 (2020).
 48. Yu, C., Li, Z., Penna, N. T. & Crippa, P. Generic atmospheric correction model for interferometric synthetic aperture radar observations. *J. Geophys. Res.: Solid Earth* **123**, 9202–9222 (2018).
 49. Tymofeyeva, E. & Fialko, Y. Geodetic evidence for a blind fault segment at the southern end of the San Jacinto Fault Zone. *J. Geophys. Res.: Solid Earth* **123**, 878–891 (2018).
 50. Sandwell, D. T. & Wessel, P. Interpolation of 2-D vector data using constraints from elasticity. *Geophys. Res. Lett.* **43**, 10,703–10,709 (2016).
 51. Okada, Y. Surface deformation due to shear and tensile faults in a half-space. *Bull. Seismol. Soc. Am.* **75**, 1135–1154 (1985).
 52. Wang, L. & Barbot, S. Three-dimensional kinematics of the India–Eurasia collision. *Commun. Earth Environ.* **4**, 164 (2023).
 53. Li, Y. et al. Slip deficit rate and seismic potential on crustal faults in Tibet. *Geophys. Res. Lett.* **52**, e2024GL112122 (2025).
 54. Wang, M. & Shen, Z.-K. Present-day crustal deformation of continental China derived from GPS and its tectonic implications. *J. Geophys. Res.: Solid Earth* **125**, e2019JB018774 (2020).
 55. Wu, Y. et al. High-precision vertical movement and three-dimensional deformation pattern of the Tibetan Plateau. *J. Geophys. Res.: Solid Earth* **127**, e2021JB023202 (2022).
 56. Barbot, S., Moore, J. D. P. & Lambert, V. Displacement and stress associated with distributed anelastic deformation in a half-space. *Bull. Seismological Soc. Am.* **107**, 821–855 (2017).
 57. Meade, B. J. Algorithms for the calculation of exact displacements, strains, and stresses for triangular dislocation elements in a uniform elastic half space. *Computers Geosci.* **33**, 1064–1075 (2007).
 58. Laske G., Masters G., Ma Z., & Pasyanos M. Update on CRUST1.0—A 1-degree global model of Earth’s crust. In: *Geophysical research abstracts* (2013).
 59. Frank, M. & Wolfe, P. An algorithm for quadratic programming. *Nav. Res. Logist. Q.* **3**, 95–110 (1956).
 60. Zeng, H., Wei, S. & Wu, W. Sources of uncertainties and artefacts in back-projection results. *Geophys. J. Int.* **220**, 876–891 (2020).
 61. Ishii, M., Shearer, P. M., Houston, H. & Vidale, J. E. Extent, duration and speed of the 2004 Sumatra–Andaman earthquake imaged by the Hi-Net array. *Nature* **435**, 933–936 (2005).
 62. Meng L., Inbal A. & Ampuero J.-P. A window into the complexity of the dynamic rupture of the 2011 Mw 9 Tohoku-Oki earthquake. *Geophys. Res. Lett.* **38**, (2011).
 63. Ji, C., Wald, D. J. & Helmerger, D. V. Source description of the 1999 Hector Mine, California, Earthquake, Part I: Wavelet domain inversion theory and resolution analysis. *Bull. Seismological Soc. Am.* **92**, 1192–1207 (2002).
 64. Zhu, L. & Helmerger, D. V. Intermediate depth earthquakes beneath the India-Tibet Collision Zone. *Geophys. Res. Lett.* **23**, 435–438 (1996).
 65. Zhu, L. & Rivera, L. A. A note on the dynamic and static displacements from a point source in multilayered media. *Geophys. J. Int.* **148**, 619–627 (2002).
 66. Wei, S., Graves, R., Helmerger, D., Avouac, J.-P. & Jiang, J. Sources of shaking and flooding during the Tohoku-Oki earthquake: a mixture of rupture styles. *Earth Planet. Sci. Lett.* **333–334**, 91–100 (2012).
 67. Haskell, N. A. Total energy and energy spectral density of elastic wave radiation from propagating faults. *Bull. Seismol. Soc. Am.* **54**, 1811–1841 (1964).
 68. Bekaert, D. P. S., Walters, R. J., Wright, T. J., Hooper, A. J. & Parker, D. J. Statistical comparison of InSAR tropospheric correction techniques. *Remote Sens. Environ.* **170**, 40–47 (2015).
 69. Bagnardi, M. & Hooper, A. Inversion of surface deformation data for rapid estimates of source parameters and uncertainties: a bayesian approach. *Geochem. Geophys. Geosyst.* **19**, 2194–2211 (2018).

Acknowledgements

Funding for this work was provided by the Chinese Academy of Sciences (Grant No. E4515401), the Tier 2 project “Integrating space geodesy and dense array seismology to reveal fundamental earthquake physics” supported by the Singapore Ministry of Education (MOE) (MOE-T2EP50124-0011), the Tier 3b project “Investigating Volcano and Earthquake Science and Technology (InVEST)” supported by the Singapore Ministry of Education (MOE) (MOE-MOET32021-0002, Component D), and the National Natural Science Foundation of China (Grant No. 42494861 and 42504005). We acknowledge Xiaofeng Liang from the Institute of Geophysics and Geology, Chinese Academy of Sciences, for valuable discussions regarding seismic tomography results. We appreciate Haipeng Luo of Southern University of Science and Technology and Shaoyang Li from the Institute of Geophysics and Geology, Chinese Academy of Sciences, for their discussions on postseismic deformation modelling. We acknowledge the Japanese Space Agency (JAXA) for providing the ALOS-2 PALSAR images to Z.M. under project ER4A2N150. We acknowledge the Strong Motion Observation Data Centre, Institute of Engineering Mechanics, China Earthquake Administration (Strong Motion Observation Data Sub-center of National Earthquake Data Centre) for providing strong motion data for this study.

Author contributions

Conceptualisation: S.W., Z.M.; Methodology: Z.M., S.W., H.C., H.Z., M.L., C.L.; Investigation: S.W., Z.M., C.L., H.C., H.Z., M.L.; Visualisation: Z.M., C.L., H.C., S.W., M.L.; Funding acquisition: S.W.; Project administration: S.W.; Supervision: S.W.; Writing—original draft: S.W., Z.M., C.L., H.C., H.Z., M.L.; Writing—review & editing: All authors.

Competing interests

The authors declare no competing interests.

Additional information

Supplementary information The online version contains supplementary material available at <https://doi.org/10.1038/s41467-025-68128-y>.

Correspondence and requests for materials should be addressed to Shengji Wei.

Peer review information *Nature Communications* thanks Yan Hu, Tim Wright and the other, anonymous, reviewer(s) for their contribution to the peer review of this work. A peer review file is available.

Reprints and permissions information is available at <http://www.nature.com/reprints>

Publisher’s note Springer Nature remains neutral with regard to jurisdictional claims in published maps and institutional affiliations.

Open Access This article is licensed under a Creative Commons Attribution-NonCommercial-NoDerivatives 4.0 International License, which permits any non-commercial use, sharing, distribution and reproduction in any medium or format, as long as you give appropriate credit to the original author(s) and the source, provide a link to the Creative Commons licence, and indicate if you modified the licensed material. You do not have permission under this licence to share adapted material derived from this article or parts of it. The images or other third party material in this article are included in the article's Creative Commons licence, unless indicated otherwise in a credit line to the material. If material is not included in the article's Creative Commons licence and your intended use is not permitted by statutory regulation or exceeds the permitted use, you will need to obtain permission directly from the copyright holder. To view a copy of this licence, visit <http://creativecommons.org/licenses/by-nc-nd/4.0/>.

© The Author(s) 2026